Enhanced pencil-beam scanning CTS leaky-wave antenna based on meander delay line

You, Yang; Lu, Yunlong; Wang, Yi; Xu, Jun; Huang, Jifu; Hong, Wei

DOI:
10.1109/LAWP.2021.3096084

Enhanced Pencil-Beam Scanning CTS Leaky-Wave Antenna Based on Meander Delay Line

Yang You, Yunlong Lu, Yi Wang, *Senior Member, IEEE*, Jun Xu, *Member, IEEE*, Jifu Huang, and Wei Hong, *Fellow, IEEE*

***Abstract*— This letter presents a millimeter-wave continuous transverse stub (CTS) leaky-wave antenna (LWA) with pencil-beam broadside radiation, high scanning-rate and low sidelobe levels (SLLs) characteristics. A parallel-plate waveguide (PPW) meander delay line is employed to control the phase constant of the proposed LWA. By adjusting the length of the TEM-mode PPW delay line, the phase difference between adjacent radiating elements can be altered, achieving flexible control of scanning-rate. Match stubs close to the radiation slots are utilized to suppress the open stopband, which help enlarge the beam scanning range. A linear source generator excited by multiple ports with amplitude tapering is employed to generate the quasi-TEM wave. Combined with additional amplitude tapering among the CTS radiation slots, low SLLs at both principal planes are realized. Experimental results show that the LWA with 12 radiation elements has a scanning range of -68° to 42° over the frequency range of 26 GHz to 34 GHz (a scanning-rate of 13.75°/GHz) with SLLs lower than 13.5 dB/16.6 dB and a peak gain of over 22.5 dBi.**

Keywords— *Leaky-wave antenna, continuous transverse stub array, millimeter wave antennas, waveguide arrays.*

I. Introduction

Leaky-wave antennas (LWAs) offer some low-cost, low profile beam scanning capabilities without complex feeding network [1]. This antenna technology has been widely used in radar, imaging, and high-speed communication systems [2], [3]. The characteristics of high gain, pencil-beam broadside radiation, high scanning-rate (defined as the ratio of scanning range to operating bandwidth) and low sidelobe levels (SLLs) are highly desired for improving overall system performances and lowering hardware requirement [4]-[7].

Recently, continuous transverse stub (CTS) antenna arrays have received great attention both in fixed beam and beam scanning applications due to their high performance [8]-[15]. The CTS LWA with multiple long slots can be used effectively for generating pencil-beam radiation patterns [16], and some CTS LWAs have been presented. However, most CTS LWAs are implemented using dielectric filled waveguides [12]-[14]. The dielectric loss affects the antenna gain and efficiency. Air-filled waveguide is a better choice for high-performance mmW system. The authors previously presented a Ka-band CTS LWA using air-filled waveguide [15]. It achieved a scanning range of -56.2° to -2° over the frequency range of 26-42 GHz and maximum peak gain of 29.2 dBi. But, broadside scanning, high scanning-rate and low SLLs at both principal planes were not tackled.

This work aims to address these enhanced performance issues in a mmW air-filled CTS LWA. The measurements and simulations have been shown to be in a good agreement, which verifies the design concept.

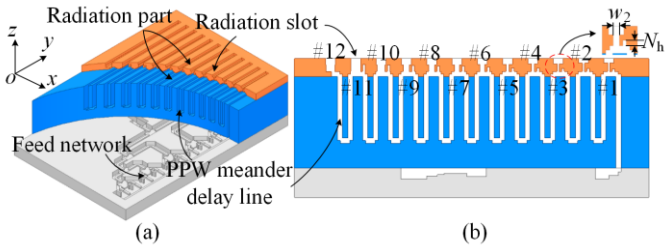

Fig. 1. Configuration of the CTS leak-wave antenna. (a) Whole structure; (b) side view.

II. Antenna Analysis and Design

The configuration of the proposed CTS LWA based on air-filled waveguide is shown in Fig. 1. It consists of a radiation part and a feed network. 12 CTS radiation slots (slot No. #1, #2, …, #12) excited through a parallel-plate-waveguide (PPW) meander delay line in series work as the radiation part. The feed network is used to generate the quasi-TEM wave to feed the radiation elements. The details are given in the following sections.

A. Open stopband suppression and beaming scanning-rate

This work was supported partly by National Key R&D Program of China under Project 2018YFB1802100, in part by National Natural Science Foundation of China under Projects 61801252, U1809203, and 61631012, in part by Zhejiang Natural Science Foundation under Project LY21F010002, Guangdong R&D Project in Key Areas under grant no. 2019B010156004, Ningbo Natural Science Foundation under Project 202003N4108 and the Fundamental Research Funds for the Provincial Universities of Zhejiang under grant no. SJLY2020001. (*Corresponding author: Yunlong Lu, Jifu Huang*)

Yang You, Yunlong Lu, and Jifu Huang are with the Faculty of Electrical Engineering and Computer Science, Ningbo University, Ningbo, Zhejiang, 315211, China (e-mail: luyunlong@nbu.edu.cn).

Yi Wang is with School of Engineering, University of Birmingham, B15 2TT, United Kingdom (e-mail: y.wang.1@bham.ac.uk).

Jun Xu is with the State Key Laboratory of Terahertz and Millimeter Waves, Department of Electrical Engineering, City University of Hong Kong, Hong Kong SAR, P. R. China.

W. Hong is with the State Key Laboratory of Millimeter Waves, School of Information Science and Engineering, Southeast University, Nanjing, 210096, P. R. China.

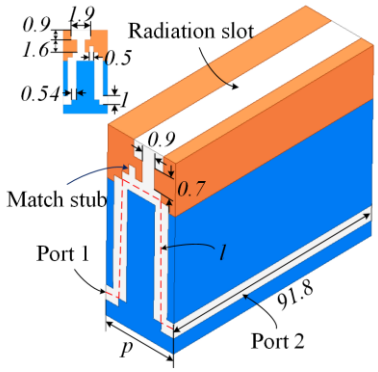

Fig. 2. CTS radiation element. All dimensions are given in millimeters.

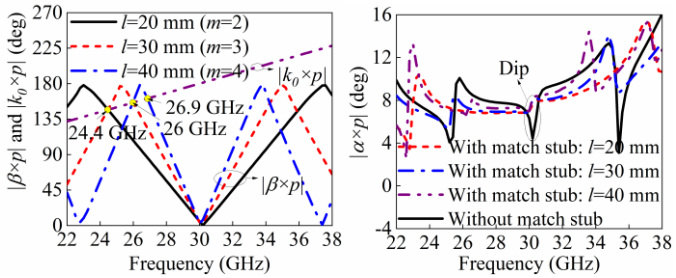

Fig. 3. Simulated dispersion diagram with different lengths of PPW meander delay line: (a) $|\beta\times p|$ and $|k_0\times p|$, (b) $|\alpha\times p|$.

Fig. 2 shows the structure of one radiation element with a period of p. It consists of a two-step flared CTS radiation slot, excited by quasi-TEM wave through the PPW meander delay line. The corner of the meander line is inverted to reduce reflection. It should be noted that the low SLL characteristics are not considered in this part. The period p is selected to avoid grating lobes and maximize scanning range [17]. Combined with the length of the meander delay line in one element (l), the beam pointing (θ) can be calculated by the following equation:

$$\frac{2\pi}{\lambda}p\sin\theta-\frac{2\pi}{\lambda_g}l=-2m\pi,\ m=1,2,3... \tag{1}$$

where λ_g is the guided wavelength in the PPW meander delay line. As a result, the beam pointing at a specific operating frequency can be adjusted by changing the length l. For broadside radiation at a desired frequency f_b, the length l can be derived from (1) as $l = m \times \lambda_{gb}$ (λ_{gb} is the guided wavelength at f_b). In this work, we set the frequency of broadside radiation to be 30 GHz ($\lambda_{gb} \approx 10$ mm for PPW here), and the period p to be $\lambda_{gb}/2$.

In order to enlarge the beam scanning range, the match stub is loaded next to the radiation slot to suppress the open stopband. Based on the optimized dimensions shown in Fig. 2, the dispersion diagram under different values of l is given in Fig. 3(a) and (b). From the phase curves, it can be seen that the operating band of the radiation element varies with l. For l=20 mm (m=2), the band is 24.4 - 37.8 GHz. This reduces to 26 - 35 GHz for l=30 mm (m=3), and 26.9 - 33.6 GHz for l=40 mm (m=4). See Fig. 3(b), the attenuation peaks at both band edges of each band. This will cause the peak gain of the main beam to drop gradually towards the band edge frequencies. At the

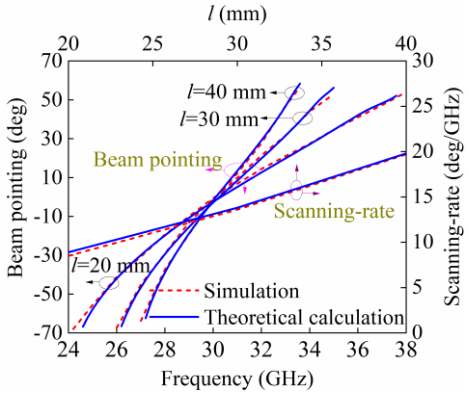

Fig. 4. Simulated beam pointing and scanning-rate with different lengths of PPW meander delay line.

frequency of the broadside radiation (30 GHz), there is an obvious dip at 30 GHz in the attenuation curve without match stub, and the attenuation curves for all values of l becomes flatter around the broadside direction when the match stub is added. This shows that irrespective of changing l, the open stopband can be well mitigated.

The beam pointing of an LWA composed of an infinite numbers of radiation elements is analyzed for different lengths of the PPW meander delay line. This can be calculated based on the phase constant and free-space wave number [17], [18]. For the different values of l, the calculated beam pointing is plotted in Fig. 4. This agrees very well with the results extracted from full-wave simulation by using HFSS. Although the operating band changes with l and the beam pointing at the start and end frequencies is slightly different, the beam scanning ranges remain around 121.5°. The calculated and simulated scanning-rates are also compared in Fig. 4. The scanning-rate of the LWA increases with the length l. This shows that the scanning-rate can be controlled by adjusting the length of meander delay line.

B. Synthesis of Radiation Patterns With Low SLLs

This section describes the method used in both E (*xoz*) - and H (*yoz*) -planes to achieve low SLLs. 12 CTS radiation elements are employed to achieve the pencil-beam, which is illustrated in Fig. 1(b). To facilitate fabrication, the length of meander delay line per element is selected to be l = 30 mm, so the operating band of the LWA is 26-35 GHz.

To achieve the low SLL in the E-plane, the amplitude distribution among the 12 radiation slots should be weighted [19]. This requires the control of the coupling from the meander delay line into the radiation slot, which can be done by adjusting the width (w_2). The change of impedance matching caused by w_2 can be resolved by optimizing N_h (marked out in Fig. 1(b)) of the match stub while keeping the open stopband suppressed. The amplitude, complied with a Taylor distribution of N=4 and SLL=-18 dB, is applied to the radiation slots. The width of radiation slot and depth of match stub are first optimized to obtain the desired amplitude distribution at 30 GHz. The values of w_2 and N_h are shown in Table I, other dimensions of each element are the same as the one shown in Fig. 2. Fig. 5(a) shows the simulated amplitude distributions among the radiation slots. It presents a quasi-Taylor

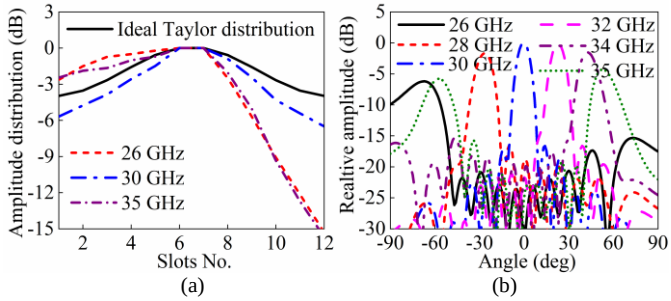

Fig. 5. (a) Simulated amplitude distribution among the radiation slots, (b) Synthesized normalized radiation pattern in E-plane.

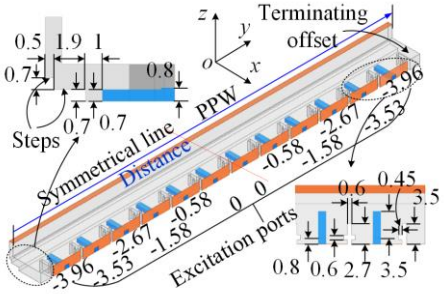

Fig. 6. Structure of multi-port excited PPW. All dimensions are given in millimeters. The normalized amplitudes at each excited port are marked out in in dB values.

TABLE I
PARAMETERS OF RADIATION SLOTS (UNIT: MM).

Slot No.	#1	#2	#3	#4	#5	#6
w_2/N_h	0.35/0.3	0.4/0.35	0.45/0.4	0.55/0.45	0.65/0.5	0.9/0.7
Slot No.	#7	#8	#9	#10	#11	#12
w_2/N_h	0.95/0.9	1.1/0.9	1.25/1	1.5/1.1	1.85/1.2	1.9/--

distribution at 30 GHz and maintains the trend of the amplitude distribution when deviating from this frequency. The synthesized radiation pattern in the E-plane is shown in Fig. 5(b). The beam scanning range of -67° to 54.5° over the frequency range (26 - 35 GHz) is achieved, and the first SLL is lower than -15 dB across the beam scanning range. Besides, it should be noted that two separated beams pointing to forward (54.5°) and backward (-56.5°) with close peak gain appear at 35 GHz. This is because the gain of the backward radiation beam gradually increases whereas the forward beam decreases, when the phase delay ($|\beta \times p|$) approaches 180°. To maintain low backward SLLs, we choose the upper operating frequency to be 34 GHz rather than 35 GHz, so the operating band is defined as 26-34 GHz.

The radiation pattern in H-plane is determined by the amplitude distributions of the quasi-TEM wave, generated from a linear source generator. In this work, the structure of a multi-port excited PPW is used, as it has a wide bandwidth and easier to implement different types of amplitude tapering. The structure, as well as the amplitude tapering (the same Taylor distribution in E-plane) among the excitation ports, are shown in Fig. 6. The amplitude responses at output port of the PPW along *y*-axis is shown in Fig. 7(a). A good amplitude tapering is achieved over the frequency range of 26-34 GHz. The fluctuation in the distribution is caused by the discrete

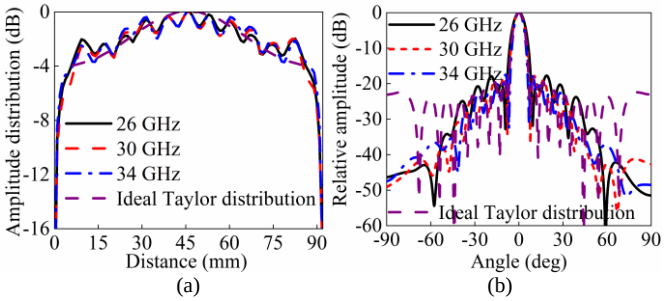

Fig. 7. (a) Ideal Taylor distribution and E-field amplitude distributions of the quasi-TEM wave in the PPW at different frequencies, (b) Radiation patterns with Taylor distribution excitation.

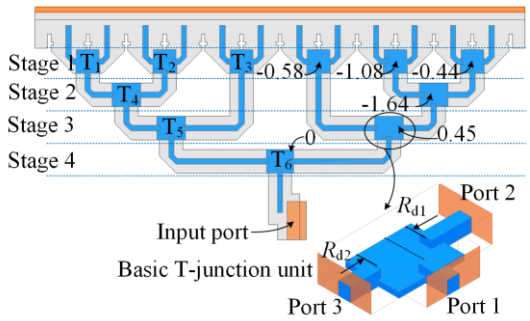

Fig. 8. Partial view of the feed structure.

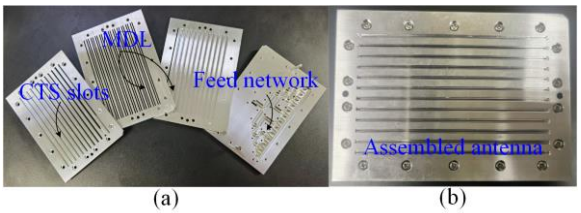

Fig. 9. Photographs of the fabricated CTS LWA. (a) Blocks, (b) Assembled antenna.

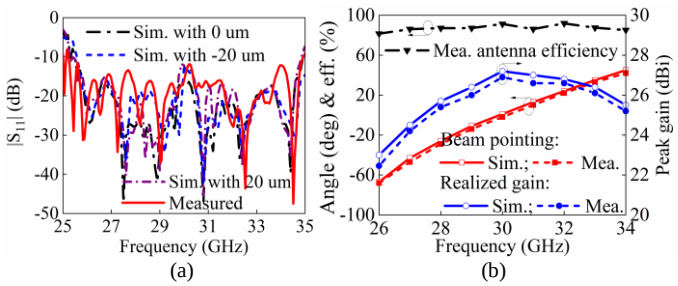

Fig. 10. Simulated and measured results. (a) $|S_{11}|$. (b) Peak gain, antenna efficiency and main beam pointing.

excitation ports. Due to short circuit reflection of metal walls, the amplitude close to the two ends of the PPW first increases and then decreases rapidly, which is inconsistent with the ideal Taylor distribution. The synthesized normalized radiation patterns in the H-plane at different frequencies is shown in Fig. 7(b). It can be seen that the first SLLs within the operating band are all below -18 dB. Compared with the theoretical radiation pattern generated by the ideal Taylor distribution excitation, the simulated SLLs are slightly higher in the range of $\theta \in$ [-45°, 45°], but much lower outside this range. This is mainly because the amplitude of the quasi-TEM wave near both ends of the PPW drops significantly, as shown in Fig. 7(a). It lowers the SLLs at the region far away from the main beam.

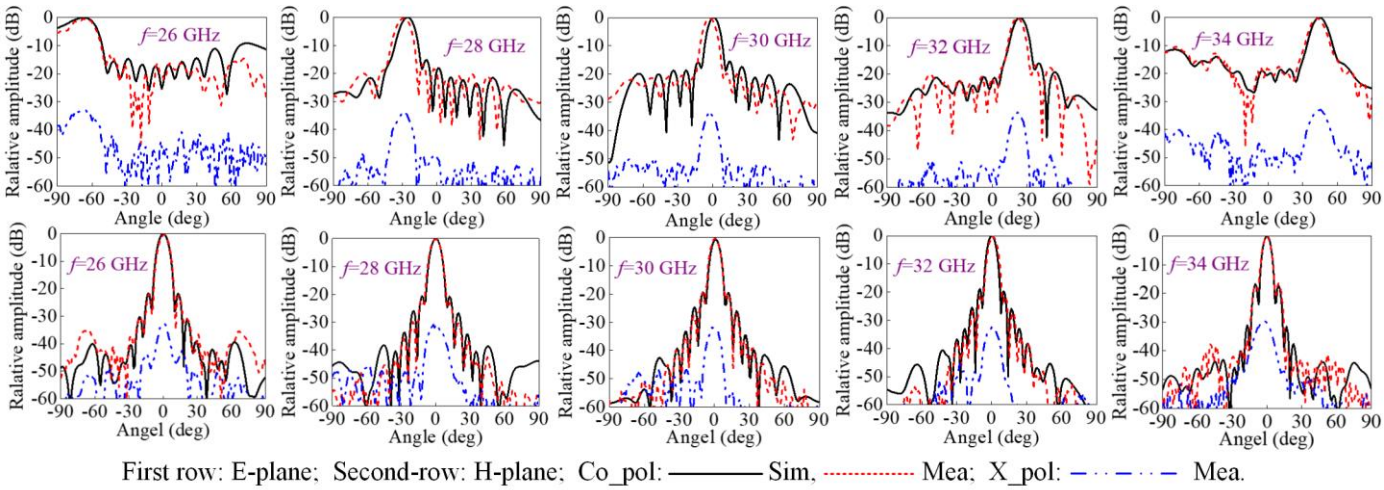

Fig. 11. Simulated and measured radiation patterns in E-plane and H-plane at different frequencies.

TABLE II
PERFORMANCES COMPARISON OF CTS LWAS

Ref.	*f* (GHz)	Beam coverage	SR	SLLs (dB)	Radiation pattern
[13]	8.5-14.1	-16.8° to 52.2°	12.3	-11.4/--	Fan-type
[14]	200-300	-75° to -30°	0.563	--/-12	Fan-type
[15]	26-42	-56.2° to -2°	3.38	-12.9/--	Pencil beam
This work	26-34	-68°to 42°	13.75	-13.5/-16.6	Pencil beam

*SR: Scanning-rate (°/GHz)

C. *Feed network*

The feed network is shown in Fig. 8. It is a 1-to-12 unequal power divider consisted of four stages of single-ridge waveguide T-junctions to satisfy the amplitude distribution given in Fig. 6. From the target amplitude distribution, the required power ratios of T-junctions in the feed network can be calculated, which are shown in Fig. 8. The power ratio used here is defined as $|S_{21}|$(dB)- $|S_{31}|$(dB). These are realized by the single-ridge H-plane T-junctions. The basic H-plane T-junction unequal power divider is also shown in Fig. 8. The different power division ratio can be realized by adjusting parameters of R_{d1} and R_{d2} [20].

III. EXPERIMENTAL RESULTS

The proposed LWA is fabricated out of aluminum by milling with tolerance of 20 um. It is divided into four blocks and assembled by using a set of screws for tightening to suppress the leakage. The photograph of fabricated prototype is shown in Fig. 9. The dimensions of the LWA is 110 mm× 77 mm × 26 mm. The radiation performances are measured in a microwave chamber and the reflection coefficient is tested by Agilent E8361C network analyzer.

Fig. 10(a) shows the simulated and measured reflection coefficients of the proposed LWA. The measure reflection coefficient is better than −11.8 dB within 26 GHz-34 GHz (26.7% fractional bandwidth) and in reasonable agreement with simulations. It should be noted that the measured $|S_{11}|$ is worse than expected at about 30 GHz (broadside radiation), but still exhibiting a good open stopband suppression. The differences come from assembly error and fabrication tolerance. The potential influence form fabrication tolerance is estimated, which is also shown in Fig. 10(a). The increased $|S_{11}|$ shown in the simulation broadly confirms the contribution of fabrication tolerance to variance. The peak gains and antenna efficiency versus operating frequency are compared in Fig. 10(b). The simulated peak gain is in the range of 23–27.2 dBi between 26 and 34 GHz, whereas the measured is 22.5–26.9 dBi. The measured antenna efficiency is between 81.5% and 91.8%. Fig. 10(b) also shows the simulated and measured main beam pointing at different frequencies. The measured beam scanning range is from -68° to 42° over 26-34 GHz. In simulation, this is from -67° to 44°. The scanning-rates are 13.75°/GHz and 13.875°/GHz for measurement and simulation, respectively.

Fig. 11 plots the simulated and measured radiation patterns in E- and H-planes at different frequencies. The pencil beam pattern is realized in the whole working frequency band. At 30 GHz, the beam pointing is slightly deviated from θ=0° due to the assembly error and fabrication tolerance. During the beam scanning, the measured SLLs remain below -13.5 dB/-16.6 dB in the E-/H-plane. The measured cross polarizations are suppressed more than 30 dB in both E- and H-planes during the beam scanning.

The performances of the proposed LWA are compared with other CTS LWAs in Table II. This work exhibits the highest scanning range and scanning-rate, while maintaining the lowest SLLs in both the E- and H-planes during beam scanning.

IV. CONCLUSION

In this letter, we demonstrated a novel Ka-band CTS LWA serially fed with a PPW meander delay line. The dispersion diagrams of the radiation element show that the open stopband can be effectively mitigated by using a match stub and the scanning-rate can be controllable by adjusting the length of meander delay line feeding the radiation slot. Amplitude tapering complied with Taylor distribution is applied in both the E- and H-plane to achieve the low SLLs when beam steering. The unique combination of these features renders this design a high-performance mmW LWA.

REFERENCES

[1] A. A. Oliner, and D. R. Jackson, "Leaky-Wave Antennas" in Antenna Engineering Handbook, 4th ed., J. Volakis, Ed. New York: McGraw-Hill, 2007.

[2] T. R. Cameron and G. V. Eleftheriades, "Experimental validation of a wideband metasurface for wide-angle scanning leaky-wave antennas," *IEEE Trans. Antennas Propag.*, vol. 65, no. 10, pp. 5245-5256, Oct. 2017.

[3] Y. J. Cheng, W. Hong, K. Wu and Y. Fan, "Millimeter-wave substrate integrated waveguide long slot leaky-wave antennas and two-dimensional multibeam applications," *IEEE Trans. Antennas Propag.*, vol. 59, no. 1, pp. 40-47, Jan. 2011.

[4] D. Zheng, Y. Lyu and K. Wu, "Longitudinally slotted SIW leaky-wave antenna for Low cross-polarization millimeter-wave applications," *IEEE Trans. Antennas Propag.*, vol. 68, no. 2, pp. 656-664, Feb. 2020.

[5] W. Cao, Z. N. Chen, W. Hong, B. Zhang and A. Liu, "A beam scanning leaky-wave slot antenna with enhanced scanning angle range and flat gain characteristic using composite phase-shifting transmission line," *IEEE Trans. Antennas Propag.*,, vol. 62, no. 11, pp. 5871-5875, Nov. 2014.

[6] D. Guan, Q. Zhang, P. You, Z. Yang, Y. Zhou and S. Yong, "Scanning rate enhancement of leaky-wave antennas using slow-wave substrate integrated waveguide structure," *IEEE Trans. Antennas Propag.*, vol. 66, no. 7, pp. 3747-3751, Jul. 2018.

[7] G. Zhang, Q. Zhang, Y. Chen and R. D. Murch, "High-scanning-rate and wide-angle leaky-wave antennas based on glide-symmetry goubau line," *IEEE Trans. Antennas Propag.*, vol. 68, no. 4, pp. 2531-2540, Apr. 2020.

[8] J. Gao, X. Lei, G.-H. Chen, Y. Zhang, and J.-M. Wu, "Design of the variable inclination continuous transverse stub antenna based on rectangular grating slow-wave structure," *Int. J. Antennas Propag.*, vol. 2018, Apr. 2018, Art. no. 5793535.

[9] T. Potelon, M. Ettorre, L. Le Coq, T. Bateman, J. Francey and R. Sauleau, "Reconfigurable CTS antenna fully integrated in PCB technology for 5G backhaul applications," *IEEE Trans. Antennas Propag.*, vol. 67, no. 6, pp. 3609-3618, June 2019.

[10] Y. Gao, T. Hong, W. Jiang, S. Gong and F. Li, "Low-profile wideband CTS array using substrate-integrated waveguide technology for K -band applications," *IEEE Trans. Antennas Propag.*, vol. 67, no. 8, pp. 5711-5716, Aug. 2019.

[11] H. Qiu, X. Yang, Y. Yu, T. Lou, Z. Yin and S. Gao, "Compact beam-dcanning flat array based on substrate-integrated waveguide," *IEEE Trans. Antennas Propag.*, vol. 68, no. 2, pp. 882-890, Feb. 2020.

[12] H. Choe and S. Lim, "Millimeter-wave continuous transverse stub (CTS) antenna array using substrate integrated waveguide (SIW) technology," *IEEE Trans. Antennas Propag.*, vol. 62, no. 11, pp. 5497–5503, Nov. 2014.

[13] X.-X. Yang, L. Di, Y. Yu, and S. Gao, "Low-profile frequency-scanned antenna based on substrate integrated waveguide," *IEEE Trans. Antennas Propag.*, vol. 65, no. 4, pp. 2051–2056, Apr. 2017.

[14] A. Gomez-Torrent et al., "A low-profile and high-gain frequency beam steering subterahertz antenna enabled by silicon micromachining," *IEEE Trans. Antennas Propag.*, vol. 68, no. 2, pp. 672-682, Feb. 2020.

[15] Y. You, Y. Lu, Q. You, Y. Wang, J. Huang and M. J. Lancaster, "Millimeter-wave high-gain frequency-scanned antenna based on waveguide continuous transverse stubs," *IEEE Trans. Antennas Propag.*, vol. 66, no. 11, pp. 6370-6375, Nov. 2018.

[16] N. Bayat-Makou, K. Wu and A. A. Kishk, "Single-layer substrate-integrated broadside leaky long-slot array sntennas with embedded reflectors for 5G systems," *IEEE Trans. Antennas Propag.*, vol. 67, no. 12, pp. 7331-7339, Dec. 2019.

[17] Y. Li, and J. Wang, "Dual-band leaky-wave antenna based on dual-mode composite microstrip line for microwave and millimeter-wave applications", *IEEE Trans. Antennas Propag.*, vol. 66, no. 4, pp. 1660-1668, Apr. 2018.

[18] Y. Geng, J. Wang, Z. Li, Y. Li, M. Chen, and Z. Zhang, "Dual-beam and tri-band SIW leaky-wave antenna with wide beam scanning range including broadside direction", *IEEE Access*, vol. 7, pp. 176361-176368, 2019.

[19] J. Liu, D. R. Jackson, Y. Li, C. Zhang, and Y. Long, "Investigations of SIW leaky-wave antenna for endfire-radiation with narrow beam and sidelobe suppression", *IEEE Trans. Antennas Propag.*, vol. 62, no. 9, pp. 4489-4497, Sep. 2014.

[20] L. Qin, Y. Lu, Q. You, Y. Wang, J. Huang, and P. Gardner, "Millimeter-wave Slotted waveguide array with unequal beamwidths and low sidelobe levels for vehicle radars and communications", *IEEE Trans. Veh. Technol.*, vol. 67, no. 11, pp. 10674-10682, Nov. 2018.